

Unleashing MLLMs on the Edge: A Unified Framework for Cross-Modal ReID via Adaptive SVD Distillation

Hongbo Jiang ^{*1} Jie Li ^{*1} Xinqi Cai ¹ Tianyu Xie ¹ Yunhang Shen ² Pingyang Dai ¹ Liujuan Cao ¹

Abstract

Practical cloud-edge deployment of Cross-Modal Re-identification (CM-ReID) faces challenges due to maintaining a fragmented ecosystem of specialized cloud models for diverse modalities. While Multi-Modal Large Language Models (MLLMs) offer strong unification potential, existing approaches fail to adapt them into a single end-to-end backbone and lack effective knowledge distillation strategies for edge deployment. To address these limitations, we propose MLLMEmbed-ReID, a unified framework based on a powerful cloud-edge architecture. First, we adapt a foundational MLLM into a state-of-the-art cloud model. We leverage instruction-based prompting to guide the MLLM in generating a unified embedding space across RGB, infrared, sketch, and text modalities. This model is then trained efficiently with a hierarchical Low-Rank Adaptation finetuning (LoRA-SFT) strategy, optimized under a holistic cross-modal alignment objective. Second, to deploy its knowledge onto an edge-native student, we introduce a novel distillation strategy motivated by the low-rank property in the teacher's feature space. To prioritize essential information, this method employs a Principal Component Mapping loss, while relational structures are preserved via a Feature Relation loss. Our lightweight edge-based model achieves state-of-the-art performance on multiple visual CM-ReID benchmarks, while its cloud-based counterpart excels across all CM-ReID benchmarks. The MLLMEmbed-ReID framework thus presents a complete and effective solution for deploying unified MLLM-level intelligence on resource-constrained devices. The code and models will be open-sourced soon.

¹Xiamen University, Media Analytics and Computing Lab, Department of Artificial Intelligence, School of Informatics, Xiamen, China ²Tencent YouTu Lab, Shanghai, China. Correspondence to: Liujuan Cao <caoliujuan@xmu.edu.cn>.

Preprint. February 16, 2026.

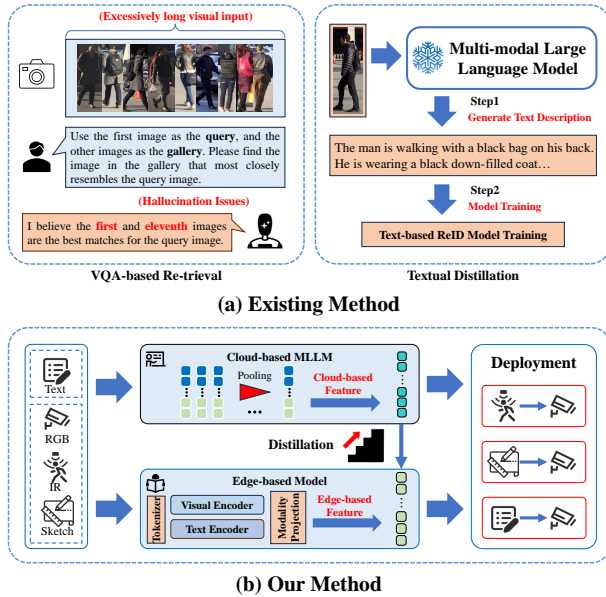


Figure 1. A Comparison of MLLM-based ReID paradigms. Images are from the QrCM-ReID dataset. (a) Existing methods indirectly apply MLLMs for VQA-based retrieval (limited by gallery size, prone to hallucination with long visual contexts) or textual distillation (restricting to text-only ReID). (b) Our MLLMEmbed-ReID directly uses a cloud-based MLLM as a unified teacher for diverse modalities. Its unified knowledge is distilled to a lightweight edge student for practical deployment.

1. Introduction

Person re-identification (ReID) (Sun et al., 2024; Wu et al., 2022) is a fundamental computer vision task for applications ranging from intelligent surveillance to public safety. While single-modal ReID (SM-ReID) (He et al., 2021) has matured, real-world systems increasingly require Cross-Modal re-identification (CM-ReID) (Jiang & Ye, 2023; Chen et al., 2022a; Zhang & Wang, 2023) capabilities, such as matching infrared to RGB images. This necessitates learning the feature that is both discriminative and modality-invariant. Concurrently, the practical deployment of ReID has converged on a cloud-edge collaborative architecture (Gu et al., 2023; Wang et al., 2024b). In this paradigm, high-capability models on cloud servers perform large-scale retrieval, while the edge models provide low-latency inference. A critical

challenge in this setting is the scalability of the cloud component, as maintaining a fragmented ecosystem of specialized, computationally-intensive models for each CM-ReID pairing is inefficient and unsustainable.

Multimodal Large Language Models (MLLMs) (Wang et al., 2025; Yang & Zhang, 2024; Lu et al., 2025; Niu et al., 2025; Bai et al., 2025), are strong candidates to resolve this by serving as a singular, unified cloud model. Prior research has explored integrating MLLMs, such as generating textual descriptions for text-based ReID or reformulating the task into a Visual Question Answering (VQA) problem. As depicted in Figure 1 (a), these existing paradigms are often indirect and suffer from practical limitations such as context length constraints and factual hallucination, or are confined to single text-based ReID tasks through textual distillation. While innovative, these approaches do not employ the MLLM as a singular, end-to-end feature extractor for diverse CM-ReID tasks. The full potential of MLLMs as a truly unified backbone thus remains underexplored. Furthermore, MLLMs’ immense size creates deployment barriers for edge devices, and conventional knowledge distillation methods are ill-suited. Experiments show conventional distillation approaches fail in the text-based ReID task. At the same time, we found that traditional distillation methods treat MLLM’s structured knowledge as a holistic black box, neglecting its internal feature attributes.

We introduce MLLM-Embed-ReID, a novel cloud-edge collaborative framework. We first propose a novel and powerful cloud-based teacher model. By adapting a foundational MLLM using a hierarchical LoRA-SFT and a composite ReID training objective, we learn a single, shared embedding space for RGB, infrared, sketch, and text modalities without any task-specific modules. During inference, this teacher model processes multimodal data via instructional prompts and extracts a globally-aware ReID feature using a pooling operation on its final hidden states. This approach establishes a new state-of-the-art for unified CM-ReID at the cloud level, providing a robust foundation of knowledge for edge deployment.

Building upon this powerful teacher, we then tackle the critical challenge of edge deployment. We introduce a novel knowledge distillation strategy based on a key empirical observation: the teacher’s ReID feature space exhibits a distinct low-rank phenomenon, with discriminative information concentrated in a small subset of principal dimensions. Leveraging Singular Value Decomposition (SVD), our method designs a structured learning curriculum that explicitly guides the lightweight student to master principal components first, while aligning feature correlations to indirectly learn vital minor dimensions. Extensive experiments demonstrate that this structured approach enables our lightweight edge model to achieve state-of-the-art perfor-

mance on visual CM-ReID tasks.

Our main contributions are threefold:

- We pioneer the end-to-end adaptation of an MLLM into a singular, unified backbone for diverse CM-ReID tasks. Our method creates a new state-of-the-art cloud model by leveraging instruction-based prompting to generate a unified embedding space across four modalities, and coupling this with a hierarchical LoRA-SFT strategy under a holistic alignment objective for efficient and effective fine-tuning.
- We discover the low-rank property in MLLM’s ReID feature space and propose a novel distillation strategy that employs Principal Component Mapping and Feature Relation losses to structure knowledge transfer for efficient edge deployment.
- We present a complete cloud-edge collaborative solution validated by comprehensive experiments, demonstrating that our lightweight edge model achieves state-of-the-art performance while maintaining the unified intelligence of MLLMs on resource-constrained devices.

2. Related Work

2.1. Cross-Modal Re-identification with Multimodal Large Language Models

The CM-ReID task aims to match identities across diverse modalities like text, sketch, infrared and RGB. IRRA (Jiang & Ye, 2023) addresses fine-grained matching in text-based ReID through implicit relation reasoning and a global alignment mechanism. SketchTransformer (Chen et al., 2022a) proposes an asymmetrical disentanglement learning method based on the Transformer architecture, utilizing dynamic synthesis-assisted sketches to mitigate cross-modal information asymmetry. DEEN (Zhang & Wang, 2023) improves CM-ReID performance under complex lighting conditions through diverse embedding expansion. While effective, this specialized approach has led to a fragmented system.

To address this, unified frameworks like TriReID (Zhai et al., 2022), AIO (Li et al., 2024), and FlexiReID (Sun et al., 2025) have demonstrated the feasibility of handling multiple CM-ReID tasks within a single model, motivating the pursuit of more scalable and flexible architectures.

In recent years, MLLMs, which integrate visual encoders with LLMs (Liu et al., 2023), have emerged as a powerful tool for ReID due to their strong cross-modal understanding. One primary application is using MLLMs to understand pedestrian images and producing rich textual descriptions for ReID. For example, HPMT (Tan et al., 2024) employs

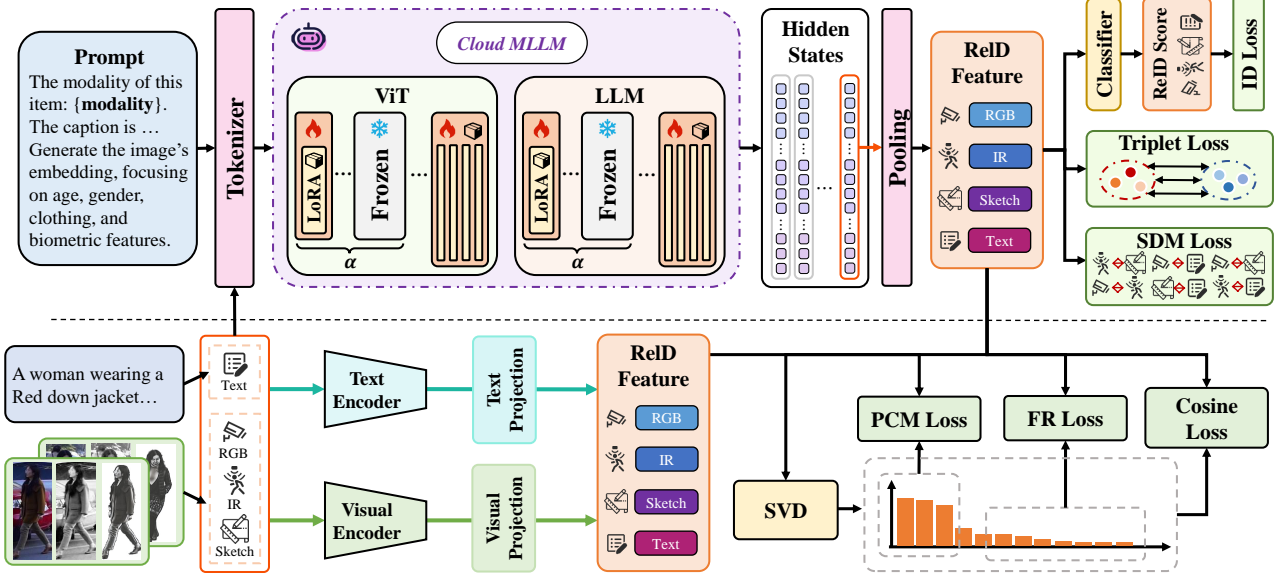


Figure 2. Overview of the proposed MLLM-Embed-ReID framework. Images are from the QrCM-ReID dataset. It primarily consists of two components: cloud model fine-tuning and edge model distillation. The cloud model includes task instructions and modality prompts, an MLLM backbone (Qwen2-VL), pooling operations, Identity Identification (ID loss), triplet learning (Triplet loss), and Similarity Distribution Matching (SDM). The edge model primarily includes Vision Language Model (VLM) backbone (CLIP (ViT-L/14)), modality projection, distillation matching loss (e.g., cosine loss), Principal Component Mapping Loss (PCM loss), and Feature Relation Loss (FR loss). Within the MLLM-Embed-ReID framework, both cloud and edge models can end-to-end unify the completion of CM-ReID tasks.

CLIP as a backbone and filters potential noise by measuring similarity between generated text and image features. HAM (Jiang et al., 2025) introduces style clustering and prompt learning to generate stylistically diverse descriptions, improving generalization in CM-ReID. Another line of research reformulates ReID as an interactive task. ChatReID (Niu et al., 2025) and LLava-ReID (Lu et al., 2025) explore interactive or multi-round dialogue mechanisms for refining text-based ReID queries. However, these methods are often not end-to-end or are confined to a single task, failing to leverage the MLLM as a unified feature extractor.

Recent works such as LVLM-ReID (Wang et al., 2024a) and MLLMReID (Yang & Zhang, 2024) demonstrate the potential of MLLMs or their components as direct feature extractors for single-modal ReID. Despite this promise, their application to a unified, multi-modal CM-ReID setting remains relatively underexplored. Furthermore, the massive computational and memory requirements of MLLMs make them infeasible for direct deployment on resource-constrained edge devices. Edge-cloud collaboration (Gu et al., 2023; Wang et al., 2024b) is a promising paradigm to address this issue, where computationally intensive inference is performed on cloud servers while lightweight models operate on edge devices for real-time processing. This motivates the need for effective knowledge distillation strategies that can transfer the rich cross-modal understanding capabilities of MLLMs to compact edge-based models suitable for edge deployment in CM-ReID systems.

2.2. Knowledge Distillation

Knowledge distillation has been widely adopted in CM-ReID to transfer knowledge from a powerful teacher model to a lightweight student model. Early approaches primarily align the output distributions of teacher and student networks using contrastive or classification-based losses (Deng et al., 2025). Beyond final outputs, several works extend the alignment to intermediate feature representations at key layers (Chen et al., 2020; Lu et al., 2020), or replicate the attention maps of the teacher model to guide the student (Shin et al., 2022). Other methods focus on enabling the student to learn relationships between samples of different modalities as captured by the teacher (Chen et al., 2022b), thereby improving modality-invariant feature learning.

Inspired by (Lee et al., 2018; Zhang et al., 2024), we explore SVD-based analysis for MLLM distillation in CM-ReID. Lee et al. (Lee et al., 2018) employ SVD to eliminate spatial redundancy and extract meaningful feature information from feature maps. SVD-KD (Zhang et al., 2024) transforms complex tensor-based knowledge into one-dimensional representations via SVD, enabling effective alignment between teacher and student model layers. Building on these works demonstrating SVD’s efficacy in identifying salient features for knowledge distillation, we analyze the cloud model’s output through SVD and discover that its feature matrix exhibits low-rank properties.

3. Method

3.1. Model Architectures

The architecture of our MLLMEmbed-ReID framework is illustrated in Figure 2. It comprises a cloud-based teacher model for unified cross-modal feature extraction (*i.e.*, RGB, infrared (IR), sketch, and text), and an edge-based student model designed for efficient inference.

Cloud-Based Teacher Model. The cloud-based model is built upon the Qwen2-VL (Wang et al., 2025), serving as a unified feature extractor. To process CM-ReID data, we format the inputs using instructional templates as shown in the upper-left of Figure 2. For instance, a text sample is formatted with the template “The modality of this item: text. The caption is {}”, while visual inputs are accompanied by the task instruction “Generate the image’s embedding, focusing on age, gender, clothing, and biometric features.” We obtain a sequence of token-wise hidden states H^c from LLM. As the hidden state of the final valid token, H_{n-1}^c encapsulates the semantic information of the entire input sequence, we extract it using the attention mask, where n here is the length of valid token-wise hidden states. It serves as the ReID feature, denoted as $f_m^c \in \mathbb{R}^d$, where m represents one of the four modalities (RGB, IR, sketch, text) and d is the feature dimension. This procedure is termed the **pooling** operation.

Edge-Based Student Model. The student model adopts the CLIP (ViT-L/14) architecture (Radford et al., 2021). As CLIP is not designed for instruction-based prompting, we input the image and text data without the instructional templates to its respective encoders. For **visual modalities** $m \in \{\text{RGB, IR, sketch}\}$, an input image I_m is partitioned into a sequence of 14×14 patches, prepended with a [CLS] token, and processed by the Vision Transformer. The output hidden state corresponding to the [CLS] token is then passed through a linear projection layer to match the dimensionality of the teacher’s feature space. This yields the final visual ReID feature. For the **text modality**, an input caption I_{text} is tokenized and bracketed by [BOS] and [EOS] tokens. The sequence is then processed by the CLIP text encoder, and the resulting representation is similarly passed through a projection layer for dimensional alignment. The final ReID features extracted from the student model are denoted as $f_m^e \in \mathbb{R}^d$.

3.2. Training of Cloud-based Model

The cloud-based model, possessing pre-trained weights with general knowledge, requires efficient fine-tuning to obtain a model capable of completing unified CM-ReID tasks end-to-end. Given the strong generalization capabilities of the foundational MLLM, we employ Low-Rank Adap-

tion (LoRA) (Hu et al., 2022) for efficient fine-tuning here. Based on the principle that higher layers capture more task-specific knowledge, we apply LoRA adapters to the final four layers of both the Vision Transformer and the LLM components. These updated parameters of the LoRA adapter can be represented as $\Delta W \in \mathbb{R}^{d \times k}$, where d denotes the input dimension size of the Linear layer and k denotes the output dimension size of the Linear layer. Then the LoRA fine-tuning of the cloud-based model can be represented as follows:

$$W' = W + \Delta W, \Delta W = BA, \quad (1)$$

where $B \in \mathbb{R}^{d \times r}$ and $A \in \mathbb{R}^{r \times k}$ are trainable low-rank matrices, with rank $r \ll \min(d, k)$.

During the supervised finetuning phase, we train the teacher model with a composite task loss, $\mathcal{L}_{\text{task}}$, designed to produce highly discriminative features. This objective combines three distinct loss functions: the ID loss (Mei et al., 2024), the triplet loss (Zhou et al., 2024; Pham & Nguyen, 2025), and the Similarity Distribution Matching (SDM) loss (Jiang & Ye, 2023). Combining ID Loss and Triplet Loss leverages the strong classification supervision of the former with the discriminative metric learning of the latter, yielding robust and highly separable feature representations for effective ReID. The ID Loss (\mathcal{L}_{id}) ensures the model accurately distinguishes different identities by minimizing cross entropy between predicted labels and the true identities of pedestrians and can be defined as:

$$\mathcal{L}_{\text{id}} = -\frac{1}{N} \sum_{i=1}^N \log \left(\frac{\exp(s_{i,y_i})}{\sum_{j=1}^C \exp(s_{i,j})} \right), \quad (2)$$

where $s_{i,j}$ is the score of the i -th sample on the j -th pedestrian-id (pid) generated by a linear classifier, and y_i is the label of the i -th sample.

The Triplet Loss (\mathcal{L}_{tri}) structures the embedding space by minimizing the distance between an anchor feature f_a and a positive feature f_p (same identity), while maximizing the distance to a negative feature f_n (different identity):

$$\mathcal{L}_{\text{tri}} = \frac{1}{N} \sum_{i=1}^N \left[\|f_a^i - f_p^i\|_2^2 - \|f_a^i - f_n^i\|_2^2 + \alpha \right]_+, \quad (3)$$

where α is a fixed margin and the function $f(z) = [z]^+ = \max(z, 0)$ is the hinge function.

To explicitly enforce robust cross-modal feature alignment and constrain their relative positions within the embedding space, we additionally minimize the SDM loss. SDM loss (\mathcal{L}_{sdm}) aligns the similarity distributions between pairs of modalities. Given a mini-batch of N m - n pairs, where m, n represent different modalities and N represents the batch size, we can construct a set of m - n ReID feature pairs $\{(f_{i,m}^c, f_{j,n}^c), y_{i,j}\}_{j=1}^N$ for each ReID feature

$f_{i,m}^c$ from modality m . If $(f_{i,m}^c, f_{j,n}^c)$ is a matched pair from the same pid, $y_{i,j} = 1$. The similarity function is $sim(\mathbf{x}, \mathbf{y}) = \mathbf{x}^\top \mathbf{y} / |\mathbf{x}| |\mathbf{y}|$ and can denote the similarity matrix between \mathcal{L}_2 normalized \mathbf{x} and \mathbf{y} . Then the probability of matching pairs can be simply calculated by

$$p_{i,j} = \frac{\exp(sim(f_{i,m}^c, f_{j,n}^c) / \tau)}{\sum_{k=1}^N \exp(sim(f_{i,m}^c, f_{k,n}^c) / \tau)}, \quad (4)$$

where τ is a temperature hyperparameter which controls the probability distribution peaks. Then the loss from modality m to modality n is computed by

$$\mathcal{L}_{m2n} = \frac{1}{N} \sum_{i=1}^N \sum_{j=1}^N p_{i,j} \log \left(\frac{p_{i,j}}{q_{i,j} + \epsilon} \right), \quad (5)$$

where $q_{i,j} = y_{i,j} / \sum_{k=1}^N y_{i,k}$ is the true matching probability. Meanwhile, conventional CM-ReID tasks typically employ SDM loss to constrain only the modality tested. However, to accurately regularize the vector space, there should be six modality constraints.

$$\mathcal{L}_{SDM} = \sum_{i=1}^6 (\mathcal{L}_{m2n}^i + \mathcal{L}_{n2m}^i). \quad (6)$$

Finally, the total task loss is the sum of these components:

$$\mathcal{L}_{task} = \mathcal{L}_{id} + \mathcal{L}_{tri} + \mathcal{L}_{SDM}. \quad (7)$$

3.3. Low-Rank Phenomenon

To develop a more effective distillation strategy than naive feature mimicry, we first analyzed the internal structure of the trained teacher model’s feature space. We collected a batch of n ReID feature vectors, forming a feature matrix $F_m^c \in \mathbb{R}^{n \times d}$, where n is the number of samples and d is the feature dimension. We then performed SVD on it:

$$F_m^c = U \Sigma V^T, \quad (8)$$

where U and V are $n \times d$ orthogonal matrices. Σ is an $n \times d$ diagonal matrix whose diagonal elements are the singular values, σ_k , ordered by magnitude.

As illustrated in Figure 3, the analysis revealed a distinct **low-rank phenomenon**. The singular values exhibit a long-tail distribution, with a small fraction of the principal components accounting for a vast majority of the cumulative variance. This indicates that the most discriminative information is concentrated within a low-dimensional subspace. To quantify the importance of each original feature dimension, we compute a weighted score based on its projection onto the principal components:

$$w_k = \frac{\sigma_k^2}{\sum_{j=1}^r \sigma_j^2}, \quad \text{importance}_i = \sum_{k=1}^d |v_{i,k}| w_k, \quad (9)$$

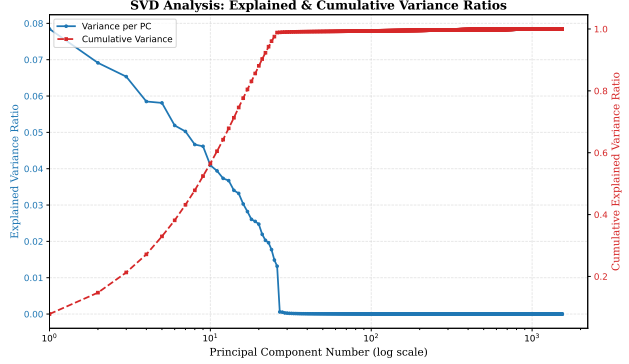


Figure 3. SVD analysis of cloud-based model’s ReID feature. The left y-axis shows the explained variance ratio per principal component, while the right y-axis shows the cumulative explained variance ratio. The x-axis is plotted on a logarithmic scale to better visualize the rapid decay of singular values.

where w_k is the normalized variance contribution of the k -th principal component, $v_{i,k}$ is the loading of the i -th original feature dimension on the k -th principal component, r is the rank of F_m^c and d is the number of the feature dimension. These importance scores also follow a long-tail distribution, further motivating a distillation strategy that prioritizes the most significant feature dimensions. To further validate the low-rank phenomenon, we conducted additional experiments across diverse datasets, as detailed in Section C. The results consistently exhibit the same patterns.

3.4. Distillation of the Edge-based Model

To deploy efficient inference models in resource-constrained edge-based computing environments, we designed a basic distillation method and subsequently improved it based on the low-rank phenomenon. The fundamental distillation method starts with directly employing a cosine comparison loss function to align the ReID feature of the cloud-based model and edge-based model. The cosine loss can be defined as

$$\mathcal{L}_{cosine} = 1 - \frac{f_m^c f_m^e}{|f_m^c| |f_m^e|}. \quad (10)$$

According to the low-rank phenomenon, we further designed two loss functions that can rapidly capture highly important features during distillation while also accommodating less significant dimensions. First, we design a **Principal Component Mapping Loss** (PCM) as follows:

$$\mathcal{L}_{pcm} = \mathcal{L}_{match}(f_m^c V^k, f_m^e V^k), \quad (11)$$

where V^k represents the first k principal components extracted from the right singular matrix obtained by performing SVD on the ReID tokens from the cloud-based model and \mathcal{L}_{match} is a distillation-based contrastive loss function, such as the cosine loss function. This means that the ReID features of the cloud and edge will be mapped to the vector

space containing the top k principal components. In this way, the edge-based model can more readily capture essential dimensional information during the distillation process.

However, ReID falls under embedding-based tasks, and in such tasks, non-essential dimensions also play an equal role in feature matching for retrieval. Therefore, we need to account for non-important dimensions, but directly calculating comparison losses for non-important dimensions would be overly cumbersome. Considering that the low-rank phenomenon we observed reflects the long-tail distribution of important dimensions, the Low-rank approximation theory implies that components corresponding to less important (lower-variance) dimensions can be effectively represented by linear combinations of the principal components. In other words, by learning the relationships between dimensions, we can indirectly account for non-important dimensions. Thus, we designed the **Feature Relation Loss** (FR) and it can be defined as follows:

$$\mathcal{L}_{fr} = \mathcal{L}_{match}(f_m^{c\top} f_m^c, f_m^{e\top} f_m^e), \quad (12)$$

where $f_m^{c\top} f_m^c$ is the relationship between features.

To validate the effectiveness of the distillation method and mitigate catastrophic forgetting during the distillation process, the total distillation loss function is defined as

$$\begin{aligned} \mathcal{L}_{distill} = & \lambda_{task} \mathcal{L}_{task} + \lambda_{cosine} \mathcal{L}_{cosine} \\ & + \lambda_{pcm} \mathcal{L}_{pcm} + \lambda_{fr} \mathcal{L}_{fr}, \end{aligned} \quad (13)$$

where λ_{task} , λ_{cosine} , λ_{pcm} and λ_{fr} are the weights of \mathcal{L}_{task} , \mathcal{L}_{cosine} , \mathcal{L}_{pcm} and \mathcal{L}_{fr} , respectively.

4. Experiment

4.1. Experimental Setup

CM-ReID Dataset. In this work, we will follow the approach outlined in (Sun et al., 2025; Zhai et al., 2022) and introduce three text-based ReID datasets CUHK-PEDES(Ding et al., 2021), ICFG-PEDES(Shen et al., 2023), and RSTPReid(Zhu et al., 2021). Subsequently, since these datasets already possess RGB and text modalities, we apply (Zhu et al., 2023) to generate sketch modalities as described in (Chen et al., 2022a). Subsequently, we will apply (Özkanoglu & Ozer, 2022) to generate infrared-visible-light image modalities. This model is trained using visible and infrared-visible image pairs, which enables it to effectively capture thermal radiation information. This modality expansion method and the processed dataset have been proven effective in relevant papers, and we refer to this expanded dataset after modal expansion as the Quadruple Cross Modal Re-identification (QrCM-ReID) dataset. By augmenting additional modalities, we construct multi-modal pedestrian data to simulate real-world conditions, enabling the ReID model to jointly address multiple CM-ReID tasks.

Evaluation Protocols. We follow standard CM-ReID evaluation protocols, using Rank-n accuracy, mean Average Precision (mAP), and mean Inverse Negative Penalty ($mINP$) to evaluate every model in MLLMEmbed-ReID.

Implementation Details. For the cloud model, we apply Qwen2-VL-2B as our backbone network. Throughout training, LoRA rank is set to 16, and the α is set to 2. We perform experiments on four NVIDIA 3090 GPUs. For edge-based models, we adopt CLIP(ViT-L/14) as our backbone network. A linear mapping layer is configured for each modality to transform vectors from the edge-based model space into a vector space aligned with the cloud-based model. The three visual modalities (RGB, IR, sketch) share a Vision Transformer visual encoder, while the text modality uses a Transformer text encoder. All parameters of the cloud-based model are frozen throughout the distillation and training process while those of the edge-based model are unfrozen. We choose the cosine loss function as \mathcal{L}_{match} . Each identity includes at least two modality groups per batch, totaling eight samples. The batch size is set to 32 per GPU, and we use four GPUs, resulting in a total batch size of 128. The images are resized to 280×140 to fit the MLLM backbone of the cloud-based model. The fine-tuned cloud-based model uses a fixed text length of 160, while the distilled edge-based model employs a fixed text length of 77 because the former has longer prompts. The AdamW optimizer is uniformly adopted. Fine-tuning experiments run for 120 epochs, while distillation runs for 60 epochs. The initial learning rate is set to 1e-5 and is decayed to a minimum learning rate of 1e-6 using a cosine scheduler. The k of PCM is a hyperparameter, with a default value of 50.

4.2. Performance Comparison

Cloud-based Model Performance. In our experiment, we first finetune the cloud-based model using the QrCM-ReID training dataset, then distill it to obtain an edge-based model. Finally, we evaluated the model’s performance when queries and galleries originated from different models to simulate real-world scenarios. Our models are tested on three cross-modal tasks: $IR \rightarrow R$, $T \rightarrow R$, and $S \rightarrow R$. Table 1 presents the performance of cloud-based and edge-based models on the QrCM-ReID test dataset. Currently, there is little work on unified CM-ReID. Only FlexiReID (Sun et al., 2025) and our work have simultaneously completed tests for three tasks. Other methods cannot jointly process the four modalities in the QrCM-ReID dataset.

For tasks $S \rightarrow R$ and $IR \rightarrow R$, our cloud-based model achieved state-of-the-art performance on all metrics across the three test sets. For example, in task $IR \rightarrow R$, our cloud model achieved R1 of 92.87 and mAP of 90.28 on the CHUK-PEDES dataset. In the ICFG-PEDES dataset, it achieved R1 of 86.77 and mAP of 59.34. In the RSTPReid

Table 1. Comparison with the state-of-the-art methods on QrCM-ReID testing datasets. Rank (R) at k accuracy (%) is reported. The best result is displayed in bold, the second-best result is underlined, and the third-best result is italicized. E2C represents using edge-based features as the query and cloud-based features as the gallery during testing. C2C and E2E follow a similar logic for their respective query and gallery feature types. Avg. indicates the average value of the mAP metric for each method across the three test sets.

Tasks	Methods	Venue	CUHK-PEDES					ICFG-PEDES					RSTPR Reid					Avg.
			R1	R5	R10	mAP	$mINP$	R1	R5	R10	mAP	$mINP$	R1	R5	R10	mAP	$mINP$	
$S \rightarrow R$	Sketch Trans+ (Chen et al., 2023b)	PAMI2023	81.39	90.61	93.54	73.72	64.72	74.83	86.75	91.52	38.64	5.68	61.37	80.15	88.29	48.94	25.73	53.77
	DALNet (Liu et al., 2024a)	AAAI2024	83.03	92.39	94.58	75.39	66.82	77.28	87.84	92.61	40.35	6.18	64.68	83.27	89.06	51.08	27.13	55.61
	UniReID (Chen et al., 2023a)	CVPR2023	84.87	-	-	78.85	68.55	77.47	-	-	40.41	6.31	65.80	-	-	51.22	27.47	56.83
	FlexiReID (Sun et al., 2025)	ICML2025	84.92	93.17	95.02	79.21	68.83	79.28	89.69	93.37	41.21	6.85	66.79	84.52	90.39	52.72	28.36	57.71
	MLLMEmbed-ReID(Ours, C2C)	-	92.87	<u>97.27</u>	98.42	<u>89.82</u>	84.21	87.36	94.05	95.63	60.39	<u>20.47</u>	86.15	94.56	96.19	74.67	54.51	74.96
	MLLMEmbed-ReID(Ours, E2E)	-	89.14	<u>95.97</u>	97.55	<u>85.23</u>	77.64	88.10	94.69	96.25	58.90	19.44	87.01	<u>95.64</u>	96.91	<u>75.82</u>	56.53	<u>73.32</u>
$IR \rightarrow R$	GUR (Yang et al., 2023)	ICCV2023	82.06	91.72	93.95	75.84	66.86	80.31	90.89	92.78	44.36	6.90	73.42	86.29	91.35	60.43	38.52	60.21
	SDCL (Yang et al., 2024)	CVPR2024	84.57	92.73	94.58	77.32	68.20	81.36	91.83	94.07	45.81	7.92	74.67	87.94	93.16	62.75	39.93	61.96
	FlexiReID	ICML2025	85.26	93.25	95.31	79.43	69.39	82.03	92.19	94.27	46.76	8.47	75.36	88.71	93.27	63.22	40.82	63.14
	MLLMEmbed-ReID(Ours, C2C)	-	92.87	<u>97.84</u>	98.62	<u>90.28</u>	85.07	<u>86.77</u>	<u>94.23</u>	<u>95.84</u>	59.34	<u>19.43</u>	<u>85.81</u>	95.28	97.06	<u>72.91</u>	<u>52.06</u>	74.18
	MLLMEmbed-ReID(Ours, E2E)	-	90.45	<u>97.04</u>	97.95	<u>87.19</u>	80.27	88.95	95.36	96.70	59.94	<u>19.94</u>	85.89	94.95	97.10	<u>75.21</u>	55.63	<u>74.11</u>
	MLLMEmbed-ReID(Ours, E2C)	-	89.00	96.61	98.18	86.74	<u>80.62</u>	82.81	93.25	95.59	56.08	18.30	85.01	<u>95.17</u>	96.97	73.31	<u>52.25</u>	72.04
$T \rightarrow R$	ViTAA (Wang et al., 2020)	ECCV2020	55.97	75.84	83.52	-	-	50.98	68.79	75.78	-	-	-	-	-	-	-	-
	DSSL (Zhu et al., 2021)	MM2021	59.98	80.41	87.56	-	-	-	-	-	-	-	32.43	55.08	63.19	-	-	-
	LBUL+BERT (Wang et al., 2022b)	MM2022	64.04	82.66	87.22	-	-	-	-	-	-	-	45.55	68.20	77.85	-	-	-
	SAF (Li et al., 2022)	ICASSP2022	64.13	82.62	88.40	58.61	-	54.86	72.13	79.13	32.76	-	44.05	67.30	76.25	36.81	-	42.73
	TIPCB (Chen et al., 2024)	NeurIPS2022	64.26	83.19	89.10	-	-	54.96	74.72	81.89	-	-	-	-	-	-	-	-
	CAIBC (Wang et al., 2022a)	MM2022	64.43	82.87	87.35	-	-	-	-	-	-	-	47.35	69.55	79.00	-	-	-
	LGUR (Shao et al., 2022)	MM2022	65.25	83.12	89.00	-	-	59.02	75.32	81.56	-	-	-	-	-	-	-	-
	LVT (Shu et al., 2022)	ECCV2022	65.59	83.11	89.21	-	-	56.04	73.60	80.22	-	-	46.70	70.00	78.80	-	-	-
	UNIReID	CVPR2023	68.71	85.93	90.84	-	-	61.28	77.40	83.16	-	-	60.25	79.85	87.10	-	-	-
	CSKT (Liu et al., 2024b)	CVPR2023	69.70	<u>86.92</u>	91.80	<u>62.74</u>	-	58.90	77.31	<u>83.56</u>	33.87	-	57.75	81.30	<u>88.35</u>	46.43	-	47.68
$T \rightarrow R$	FlexiReID	ICML2025	69.20	<u>86.43</u>	<u>91.41</u>	62.47	48.32	61.34	78.41	83.92	35.73	7.53	55.79	79.62	86.48	45.37	26.25	47.86
	MLLMEmbed-ReID(Ours, C2C)	-	65.29	82.22	87.56	62.92	52.11	<u>59.49</u>	76.36	82.07	41.52	<u>12.10</u>	<u>59.28</u>	<u>79.89</u>	87.30	50.96	<u>31.76</u>	51.80
	MLLMEmbed-ReID(Ours, E2E)	-	57.29	75.47	82.90	55.65	44.49	54.35	70.64	77.03	37.46	<u>11.15</u>	54.01	74.12	83.90	47.29	<u>30.72</u>	46.80
	MLLMEmbed-ReID(Ours, E2C)	-	58.80	77.35	84.98	58.03	47.87	52.79	71.32	77.98	38.18	<u>11.68</u>	52.79	74.18	82.89	<u>46.44</u>	28.82	47.55

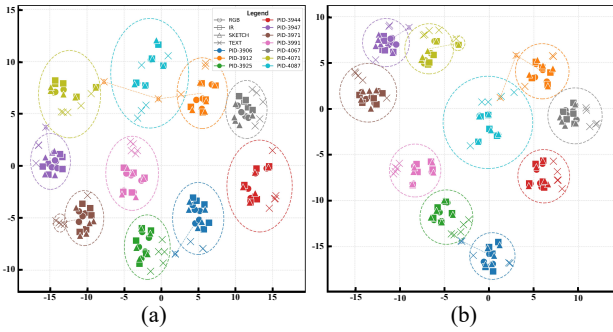


Figure 4. (a) and (b) represent the t-SNE visualization of the cloud-based model and edge-based model, respectively. Scatter points of different shapes represent different modal data. Different scatter colors represent different pedestrian IDs.

dataset, R1 reached 85.81 and mAP reached 72.91.

In $T \rightarrow R$, our cloud-based model achieved SOTA state-of-the-art levels on mAP , while Rank-n accuracy approaches state-of-the-art levels. As shown in the Figure 4 and Figure 5, through t-SNE and case analysis, we find that the cloud-based model primarily lacks the ability to perceive local information due to the absence of customized modules like Mixture of Experts (MoE) in FlexiReID (Sun et al., 2025). However, higher mAP performance demonstrates that our cloud-based model exhibits stronger comprehensive retrieval capabilities and higher generalization performance but lacks fine-grained constraints on the most accurate retrieval target.

Edge-based Model Performance. Our edge-based model



Figure 5. (a) and (b) represent the recognition results of the cloud-based model and edge-based model, respectively. Images are from the QrCM-ReID dataset. (1) and (2) represent the $IR \rightarrow R$ and $S \rightarrow R$ tasks, respectively, while (3) and (4) correspond to the $T \rightarrow R$ task. Caption A: This woman is a ponytail, wearing a black down jacket, black trousers, black boots, wearing a purple scarf and glasses. She walks with her hand in her pocket. Caption B: This woman is wearing a black coat, black trousers and black shoes. She was wearing glasses and a purple scarf. She walks while watching her cell phone.

delivers CM-ReID performance on par with cloud-based MLLM. For tasks $S \rightarrow R$ and $IR \rightarrow R$, the edge-based model continues to achieve state-of-the-art performance. For instance, in task $S \rightarrow R$, the edge-based model achieves R1 of 89.14 and mAP of 85.23 on CUHK-PEDES. On the ICFG-PEDES dataset, it achieved R1 of 88.10 and mAP of 58.90. On the RSTPR Reid dataset, R1 achieved 87.01 and mAP reached 75.82. For task $T \rightarrow R$, the edge-based model surpassed all existing methods in mAP on both ICFG-PEDES and RSTPR Reid, while its rank-n accuracy closely approached the state-of-the-art.

Table 2. Ablation study about each component of edge-based Model distillation on CUHK-PEDES. Avg. here represents the average *mAP* across all experiments for the three tasks in CUHK-PEDES.

Components	cosine	PCM	FR	IR \rightarrow R					T \rightarrow R					S \rightarrow R					Avg.
				R1	R5	R10	<i>mAP</i>	<i>mINP</i>	R1	R5	R10	<i>mAP</i>	<i>mINP</i>	R1	R5	R10	<i>mAP</i>	<i>mINP</i>	
(a) Edge-training-only				83.63	93.92	96.69	80.90	73.00	46.08	68.11	77.89	46.98	36.42	84.33	93.74	95.89	80.67	72.44	69.50
(b) (a)+cosine	\checkmark ($\lambda = 0.99$)			89.34	96.17	97.51	85.58	78.06	49.50	67.94	76.38	48.43	37.99	87.16	95.26	97.14	83.28	75.35	72.43
(c) (b)+FR	\checkmark ($\lambda = 0.29$)	\checkmark ($\lambda = 0.70$)		90.52	96.96	98.14	87.42	80.68	57.22	75.46	83.12	55.63	44.33	89.39	95.97	97.4	85.42	77.91	76.16
(d) (b)+PCM	\checkmark ($\lambda = 0.29$)	\checkmark ($\lambda = 0.70$)		90.97	97.30	98.26	87.71	80.97	57.01	75.12	82.34	55.70	44.89	89.31	96.37	97.66	85.56	78.19	76.26
(e) (b)+PCM+FR	\checkmark ($\lambda = 0.29$)	\checkmark ($\lambda = 0.35$)	\checkmark ($\lambda = 0.35$)	90.45	97.04	97.95	87.19	80.27	57.29	75.47	82.90	55.65	44.49	89.14	95.97	97.55	85.23	77.64	76.02

Table 3. Ablation Study on LoRA rank and target module parameters α on CUHK-PEDES. Avg. here represents the average *mAP* across all experiments for the three tasks in CUHK-PEDES.

LoRA Rank	α	Avg.
8	1	69.41
8	2	66.92
8	4	60.01
16	1	77.26
16	2	80.87
16	4	78.69

4.3. Ablation Study

To observe the effects of different distillation functions during the edge-based model distillation process, the results of ablation experiment are shown as the Table 2. To prevent the task loss from dominating and potentially perturbing the distillation dynamics, we maintain $\lambda_{task} = 0.01$ at a significantly low scale. We normalize the distillation loss weights such that $\lambda_{task} + \lambda_{cosine} + \lambda_{pcm} + \lambda_{fr} = 1$, which ensures a stable gradient scale during the convergence process. As illustrated by the partial tuning results in Section A, the current design is the culmination of extensive hyperparameter optimization.

In configuration (a), the edge-based model is trained without the distillation method. Configuration (b) employs a traditional alignment method, aligning the ReID feature of the edge-based model with that of the cloud-based model using a cosine similarity loss function. Configuration (c) and (d) incorporate FR and PCM respectively, building upon the foundation of configuration (b). Configuration (e) simultaneously employs both PCM and FR to investigate their performance when assigned equal weights. We assign an extremely low weight of $\lambda=0.01$ to \mathcal{L}_{task} . The sum of the other distillation loss weights should be 0.99, where the baseline cosine loss weight is set to 0.29, and both weights of FR and PCM are 0.35. This approach prevents catastrophic forgetting during the distillation. As we anticipated, configuration (c) and (d) confirmed that both losses derived from our discovery of low-rank linearity indeed deliver more efficient distillation results. Configuration (e) shows PCM and FR significantly improve the performance of the $T \rightarrow R$ task.

However, it is worth noting that when PCM and FR are combined, as demonstrated in configuration (e), no significant improvement was achieved compared to configuration (c)

and (d), and even a slight decline was observed. As shown in Section B, although combining the two distillation loss functions leads to a slight decrease in the testing metrics, it significantly enhances training efficiency. Furthermore, the observed performance decline suggests a conflict between PCM’s targeted alignment and FR’s holistic regularization. While PCM focuses the student on the low-rank subspace containing the principal components, FR enforces mimicry of the entire feature correlation matrix. This creates competing signals for the lightweight student, potentially forcing a sub-optimal trade-off that slightly compromises the learning of the most salient features.

4.4. Hyper-Parameter Analysis

To precisely control the fine-tuning depth and evaluate its impact, we varied the LoRA rank (using values of 8 and 16) and the selection of target modules for adaptation.

As detailed in Section 3, we implemented a hierarchical LoRA strategy. Adapters were applied densely to the final 4 layers of the Vision Transformer and LLM, and more sparsely to every α -th preceding layer ($\alpha \in \{1, 2, 4\}$). This approach focuses adaptation on task-specific upper layers while preserving the model’s foundational pre-trained knowledge in the lower layers.

The results in Table 3 validate this strategy, with the optimal performance on CUHK-PEDES achieved at a LoRA Rank of 16 and $\alpha = 2$. Notably, the performance degrades when $\alpha = 1$, indicating that an overly dense application of LoRA adapters is counterproductive, likely by disrupting valuable pre-trained features in the lower layers.

5. Conclusion

We present MLLM-Embed-ReID, a unified framework for cross-modal ReID that achieves state-of-the-art performance by adapting a MLLM after a hierarchical LoRA SFT as a powerful teacher. To bridge this model to resource-constrained devices, we introduce an efficient distillation strategy based on the key insight that the teacher’s feature space exhibits a low-rank property. Validated on multiple challenging benchmarks, our method delivers a highly practical and scalable cloud-edge pipeline for deploying MLLM-level intelligence efficiently on edge devices, setting a new paradigm for cloud-edge, versatile, and MLLM-based CM-ReID.

Impact Statement

This paper presents work aimed at advancing the field of Machine Learning, particularly in cross-modal representation learning for person re-identification (ReID). Our framework has potential applications in intelligent surveillance and public safety. We acknowledge that such technologies carry inherent ethical considerations, including privacy concerns and the potential for algorithmic bias. These implications are well-established in the deployment of AI-powered identification systems. While these aspects are critical, they align with the broader discourse in the field; thus, we do not believe a substantial discussion is required here beyond this acknowledgment. We advocate for the responsible development and ethical deployment of ReID technologies.

References

Bai, S., Chen, K., Liu, X., Wang, J., Ge, W., Song, S., Dang, K., Wang, P., Wang, S., Tang, J., et al. Qwen2. 5-vl technical report. *arXiv preprint arXiv:2502.13923*, 2025.

Chen, C., Ye, M., Qi, M., and Du, B. Sketch transformer: Asymmetrical disentanglement learning from dynamic synthesis. In *proceedings of the 30th ACM international conference on multimedia*, pp. 4012–4020, 2022a.

Chen, C., Ye, M., and Jiang, D. Towards modality-agnostic person re-identification with descriptive query. In *Proceedings of the IEEE/CVF conference on computer vision and pattern recognition*, pp. 15128–15137, 2023a.

Chen, C., Ye, M., Qi, M., and Du, B. Sketchtrans: Disentangled prototype learning with transformer for sketch-photo recognition. *IEEE Transactions on Pattern Analysis and Machine Intelligence*, 46(5):2950–2964, 2023b.

Chen, J., Guo, L., Sun, J., Shao, S., Yuan, Z., Lin, L., and Zhang, D. Eve: Efficient vision-language pre-training with masked prediction and modality-aware moe. In *Proceedings of the AAAI Conference on Artificial Intelligence*, volume 38, pp. 1110–1119, 2024.

Chen, Y., Zhang, S., and Qi, Z. Maenet: Boosting feature representation for cross-modal person re-identification with pairwise supervision. In *Proceedings of the 2020 International Conference on Multimedia Retrieval*, pp. 442–449, 2020.

Chen, Z., Li, Z., Zhang, S., Fang, L., Jiang, Q., and Zhao, F. Bevdistill: Cross-modal bev distillation for multi-view 3d object detection. *arXiv preprint arXiv:2211.09386*, 2022b.

Deng, S., Yuan, K., Schaefer, G., Zhou, S., Vogiatzis, G., Wang, Y., and Fang, H. A dual-aligned knowledge self-distillation framework for visible-infrared cross-modal person re-identification. *Knowledge-Based Systems*, pp. 114525, 2025.

Ding, Z., Ding, C., Shao, Z., and Tao, D. Semantically self-aligned network for text-to-image part-aware person re-identification. *arXiv preprint arXiv:2107.12666*, 2021.

Fouad, M. A., Hamza, H. M., and Hosny, K. M. Comparative analysis of fine-tuned pre-trained models for person re-identification on the market-1501 dataset. *International Journal of Computers and Informatics (Zagazig University)*, 9:94–105, 2025.

Gu, H., Zhao, L., Han, Z., Zheng, G., and Song, S. Ai-enhanced cloud-edge-terminal collaborative network: Survey, applications, and future directions. *IEEE Communications Surveys & Tutorials*, 26(2):1322–1385, 2023.

He, S., Luo, H., Wang, P., Wang, F., Li, H., and Jiang, W. Transreid: Transformer-based object re-identification. In *Proceedings of the IEEE/CVF international conference on computer vision*, pp. 15013–15022, 2021.

Hu, E. J., Shen, Y., Wallis, P., Allen-Zhu, Z., Li, Y., Wang, S., Wang, L., Chen, W., et al. Lora: Low-rank adaptation of large language models. *ICLR*, 1(2):3, 2022.

Jiang, D. and Ye, M. Cross-modal implicit relation reasoning and aligning for text-to-image person retrieval. In *Proceedings of the IEEE/CVF conference on computer vision and pattern recognition*, pp. 2787–2797, 2023.

Jiang, J., Ding, C., Tan, W., Wang, J., Tao, J., and Xu, X. Modeling thousands of human annotators for generalizable text-to-image person re-identification. In *Proceedings of the Computer Vision and Pattern Recognition Conference*, pp. 9220–9230, 2025.

Lee, S. H., Kim, D. H., and Song, B. C. Self-supervised knowledge distillation using singular value decomposition. In *Proceedings of the European conference on computer vision (ECCV)*, pp. 335–350, 2018.

Li, H., Ye, M., Zhang, M., and Du, B. All in one framework for multimodal re-identification in the wild. In *Proceedings of the IEEE/CVF Conference on Computer Vision and Pattern Recognition*, pp. 17459–17469, 2024.

Li, S., Cao, M., and Zhang, M. Learning semantic-aligned feature representation for text-based person search. In *ICASSP 2022-2022 IEEE International Conference on Acoustics, Speech and Signal Processing (ICASSP)*, pp. 2724–2728. IEEE, 2022.

Liu, H., Li, C., Wu, Q., and Lee, Y. J. Visual instruction tuning. *Advances in neural information processing systems*, 36(1):34892–34916, 2023.

Liu, X., Cheng, X., Chen, H., Yu, H., and Zhao, G. Differentiable auxiliary learning for sketch re-identification. In *Proceedings of the AAAI Conference on Artificial Intelligence*, volume 38, pp. 3747–3755, 2024a.

Liu, Y., Li, Y., Liu, Z., Yang, W., Wang, Y., and Liao, Q. Clip-based synergistic knowledge transfer for text-based person retrieval. In *ICASSP 2024-2024 IEEE International Conference on Acoustics, Speech and Signal Processing (ICASSP)*, pp. 7935–7939. IEEE, 2024b.

Lu, Y., Wu, Y., Liu, B., Zhang, T., Li, B., Chu, Q., and Yu, N. Cross-modality person re-identification with shared-specific feature transfer. In *Proceedings of the IEEE/CVF conference on computer vision and pattern recognition*, pp. 13379–13389, 2020.

Lu, Y., Yang, M., Peng, D., Hu, P., Lin, Y., and Peng, X. Llava-reid: Selective multi-image questioner for interactive person re-identification. *arXiv preprint arXiv:2504.10174*, 2025.

Mei, C., You, X., Teng, S., and LYU, X. Tl-reid: Tight-loose pairwise loss for object re-identification. In *Chinese Conference on Pattern Recognition and Computer Vision (PRCV)*, pp. 172–185. Springer, 2024.

Niu, K., Yu, H., Zhao, M., Fu, T., Yi, S., Lu, W., Li, B., Qian, X., and Xue, X. Chatreid: Open-ended interactive person retrieval via hierarchical progressive tuning for vision language models. *arXiv preprint arXiv:2502.19958*, 2025.

Özkanoğlu, M. A. and Ozer, S. Infragan: A gan architecture to transfer visible images to infrared domain. *Pattern Recognition Letters*, 155:69–76, 2022.

Pham, D. H. and Nguyen, H. N. Scm-reid: enhancing person re-identification by supervised contrastive–metric learning and hybrid loss optimization. *Journal of Electronic Imaging*, 34(4):043001–043001, 2025.

Radford, A., Kim, J. W., Hallacy, C., Ramesh, A., Goh, G., Agarwal, S., Sastry, G., Askell, A., Mishkin, P., Clark, J., et al. Learning transferable visual models from natural language supervision. In *International conference on machine learning*, pp. 8748–8763. PMLR, 2021.

Shao, Z., Zhang, X., Fang, M., Lin, Z., Wang, J., and Ding, C. Learning granularity-unified representations for text-to-image person re-identification. In *Proceedings of the 30th ACM international conference on multimedia*, pp. 5566–5574, 2022.

Shen, F., Shu, X., Du, X., and Tang, J. Pedestrian-specific bipartite-aware similarity learning for text-based person retrieval. In *Proceedings of the 31st ACM International Conference on Multimedia*, pp. 8922–8931, 2023.

Shin, S., Lee, J., Lee, J., Yu, Y., and Lee, K. Teaching where to look: Attention similarity knowledge distillation for low resolution face recognition. In *European Conference on Computer Vision*, pp. 631–647. Springer, 2022.

Shu, X., Wen, W., Wu, H., Chen, K., Song, Y., Qiao, R., Ren, B., and Wang, X. See finer, see more: Implicit modality alignment for text-based person retrieval. In *European Conference on Computer Vision*, pp. 624–641. Springer, 2022.

Sun, Z., Wang, X., Zhang, Y., Song, Y., Zhao, J., Xu, J., Yan, W., and Lv, C. A comprehensive review of pedestrian re-identification based on deep learning. *Complex & Intelligent Systems*, 10(2):1733–1768, 2024.

Sun, Z., Tan, L., Shen, Y., Cai, C., Sun, X., Dai, P., Cao, L., and Ji, R. Flexireid: Adaptive mixture of expert for multi-modal person re-identification. In *Proceedings of the 42nd International Conference on Machine Learning*, pp. 57680–57693, 2025.

Tan, W., Ding, C., Jiang, J., Wang, F., Zhan, Y., and Tao, D. Harnessing the power of mllms for transferable text-to-image person reid. In *Proceedings of the IEEE/CVF Conference on Computer Vision and Pattern Recognition*, pp. 17127–17137, 2024.

Wang, Q., Li, B., and Xue, X. When large vision-language models meet person re-identification. *arXiv preprint arXiv:2411.18111*, 2024a.

Wang, W., Tian, Y., Yang, L., Wang, H., and Yan, X. Open-qwen2vl: Compute-efficient pre-training of fully-open multimodal llms on academic resources. *arXiv preprint arXiv:2504.00595*, 2025.

Wang, Y., Yang, C., Lan, S., Zhu, L., and Zhang, Y. End-edge-cloud collaborative computing for deep learning: A comprehensive survey. *IEEE Communications Surveys & Tutorials*, 26(4):2647–2683, 2024b.

Wang, Z., Fang, Z., Wang, J., and Yang, Y. Vitaa: Visual-textual attributes alignment in person search by natural language. In *European conference on computer vision*, pp. 402–420. Springer, 2020.

Wang, Z., Zhu, A., Xue, J., Wan, X., Liu, C., Wang, T., and Li, Y. Caibc: Capturing all-round information beyond color for text-based person retrieval. In *Proceedings of the 30th ACM international conference on multimedia*, pp. 5314–5322, 2022a.

Wang, Z., Zhu, A., Xue, J., Wan, X., Liu, C., Wang, T., and Li, Y. Look before you leap: Improving text-based person retrieval by learning a consistent cross-modal common manifold. In *Proceedings of the 30th ACM international conference on multimedia*, pp. 1984–1992, 2022b.

Wu, D., Huang, H., Zhao, Q., Zhang, S., Qi, J., and Hu, J. Overview of deep learning based pedestrian attribute recognition and re-identification. *Helijon*, 8(12), 2022.

Yang, B., Chen, J., and Ye, M. Towards grand unified representation learning for unsupervised visible-infrared person re-identification. In *Proceedings of the IEEE/CVF International Conference on Computer Vision*, pp. 11069–11079, 2023.

Yang, B., Chen, J., and Ye, M. Shallow-deep collaborative learning for unsupervised visible-infrared person re-identification. In *Proceedings of the IEEE/CVF Conference on Computer Vision and Pattern Recognition*, pp. 16870–16879, 2024.

Yang, S. and Zhang, Y. Mllmreid: multimodal large language model-based person re-identification. *arXiv preprint arXiv:2401.13201*, 2024.

Zhai, Y., Zeng, Y., Cao, D., and Lu, S. Trireid: Towards multi-modal person re-identification via descriptive fusion model. In *Proceedings of the 2022 International Conference on Multimedia Retrieval*, pp. 63–71, 2022.

Zhang, J., Gao, Y., Zhou, M., Liu, R., Cheng, X., Nikolić, S. V., and Chen, S. Svd-kd: Svd-based hidden layer feature extraction for knowledge distillation. Available at SSRN 4794781, 2024.

Zhang, Y. and Wang, H. Diverse embedding expansion network and low-light cross-modality benchmark for visible-infrared person re-identification. In *Proceedings of the IEEE/CVF conference on computer vision and pattern recognition*, pp. 2153–2162, 2023.

Zheng, Y., Huge, J., and Shen, M. Modality-parallel disentanglement and contrastive optimization for efficient visible-infrared person re-identification. In *2025 4th International Conference on Image Processing, Computer Vision and Machine Learning (ICICML)*, pp. 640–644. IEEE, 2025.

Zhou, H., Qin, Q., Hou, J., Dai, J., Huang, L., and Zhang, W. Deep global semantic structure-preserving hashing via corrective triplet loss for remote sensing image retrieval. *Expert Systems with Applications*, 238:122105, 2024.

Zhu, A., Wang, Z., Li, Y., Wan, X., Jin, J., Wang, T., Hu, F., and Hua, G. Dssl: Deep surroundings-person separation learning for text-based person retrieval. In *Proceedings of the 29th ACM international conference on multimedia*, pp. 209–217, 2021.

Zhu, T., Chen, J., Zhu, R., and Gupta, G. Stylegan3: generative networks for improving the equivariance of translation and rotation. *arXiv preprint arXiv:2307.03898*, 2023.

Table 4. Sensitivity analysis of distillation objective coefficients on the CUHK-PEDES dataset. (c) allocates more weight to distillation (L_{pcm} and L_{fr}), achieving the best performance.

Components	IR \rightarrow R					T \rightarrow R					S \rightarrow R					Avg.
	R1	R5	R10	mAP	mINP	R1	R5	R10	mAP	mINP	R1	R5	R10	mAP	mINP	
(a)	88.37	95.80	97.48	84.54	76.79	51.92	66.10	73.56	46.94	36.68	86.49	95.06	96.91	82.54	74.43	71.34
(b)	89.71	96.91	97.98	86.65	79.79	53.16	72.68	80.54	52.45	41.87	88.27	95.87	97.31	84.49	76.78	74.53
(c)	90.45	97.04	97.95	87.19	80.27	57.29	75.47	82.90	55.65	44.49	89.14	95.97	97.55	85.23	77.64	76.02

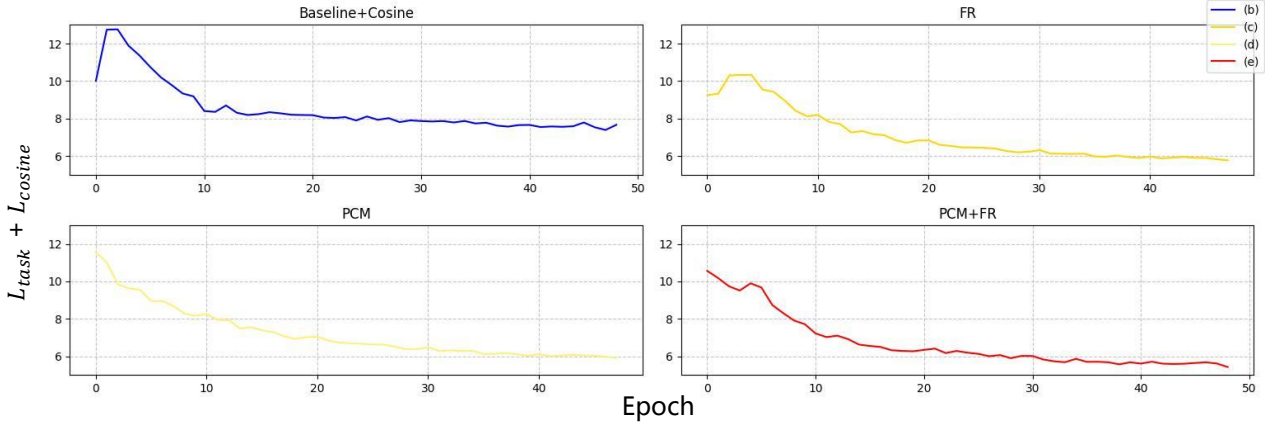


Figure 6. Convergence analysis of different distillation configurations. The Y-axis represents the shared loss ($L_{task} + L_{cos}$) to ensure a fair comparison across all schemes. Our joint configuration (e) demonstrates better optimization stability and a faster convergence rate.

A. Impact of Distillation Objective Coefficients

We have already mentioned that we maintain $\lambda_{task} = 0.01$ at a significantly low scale and $\lambda_{task} + \lambda_{cosine} + \lambda_{pcm} + \lambda_{fr} = 1$. Then, we design 3 configurations for the ratio of λ_{cosine} and $(\lambda_{pcm} + \lambda_{fr})$, denoted as (a)0.70:0.29;(b)0.495:0.495;(c)0.29:0.70. Across all configurations, we maintain equal weights for λ_{pcm} and λ_{fr} , reflecting our premise that these two distillation objectives are of equivalent importance in reshaping the model’s feature space.

As reported in Table 4, the experimental results on CUHK-PEDES demonstrate that (c) achieves the superior performance across all evaluation metrics. Compared with (a), which prioritizes global semantic alignment, (c) effectively captures the fine-grained low-rank features from the MLLM by significantly increasing the weighting intensity of the structural distillation components. This leads to a substantial improvement in Rank-1 accuracy and mAP, thereby validating the superiority of the current 29:70 ratio design.

B. Convergence Analysis: Mutual Reinforcement of Distillation Objectives

As shown in row (e) of Table 2, no significant improvement was achieved compared to configuration (c) and (d), and even a slight decline was observed. Although the joint effect of the two distillation loss functions does not yield a substantial further improvement in final accuracy, as illustrated in Figure 6, the combination of L_{pcm} and L_{uni} (FR) significantly enhances the training dynamics. Specifically, "PCM+FR" exhibits a more stable convergence trajectory with fewer initial fluctuations and achieves a faster reduction in the shared objective compared to the individual components. We select the sum of task loss and cosine loss as the evaluation metric for this analysis because they represent the primary optimization targets common to all configurations, providing a fair and consistent baseline to observe how auxiliary structural distillation objectives facilitate the overall learning process.

C. Generality of the Low-Rank Phenomenon

To further validate the low-rank phenomenon, we conduct extensive experiments across multiple independent datasets including CUHKPEDES, ICFGPEDES, RSTPReid, LLCM (Zhang & Wang, 2023), SYSU-MM01 (Zheng et al., 2025) and Market1501 (Fouad et al., 2025). Following the exact experimental protocol described in Section 3, we perform 4 randomized trials for each dataset to eliminate the potential bias of specific samples. As illustrated in Figure 7, the singular value distributions across diverse datasets consistently mirror the patterns observed in Figure 3. Due to the high consistency observed across the four randomized trials, we present only one representative result in the visualization for conciseness and better layout. Despite the variations in data domain and distribution, the inherent low-rank structure remains remarkably stable. This empirical evidence suggests that the low-rank phenomenon is a fundamental characteristic of MLLM embeddings, rather than an artifact of a specific dataset or sampling noise.

D. Edge Device Deployment Performance Validation

To address potential concerns regarding the practical feasibility of edge deployment, we conducted a performance evaluation on TWOWIN TW-T208. The experimental setup includes: GPU acceleration, bfloat16 precision, image size of 392×140 pixels, and Flash Attention2 disabled. We evaluated our distilled edge model under two scenarios: real-time single-sample processing (BatchSize=1) and batch processing (BatchSize=4). The results of the report are shown in Table 5

Table 5. Inference Performance (Latency and Throughput) report of the edge model on TWOWIN TW-T208. The evaluation metrics, latency and throughput, are measured in milliseconds (ms) and Samples Per Second (SPS), respectively.

Running Type	Batch Size	Latency (ms)	Throughput (SPS)
Real-time Processing	1	194.73	5.14
Batch Processing	4	576.67	6.94

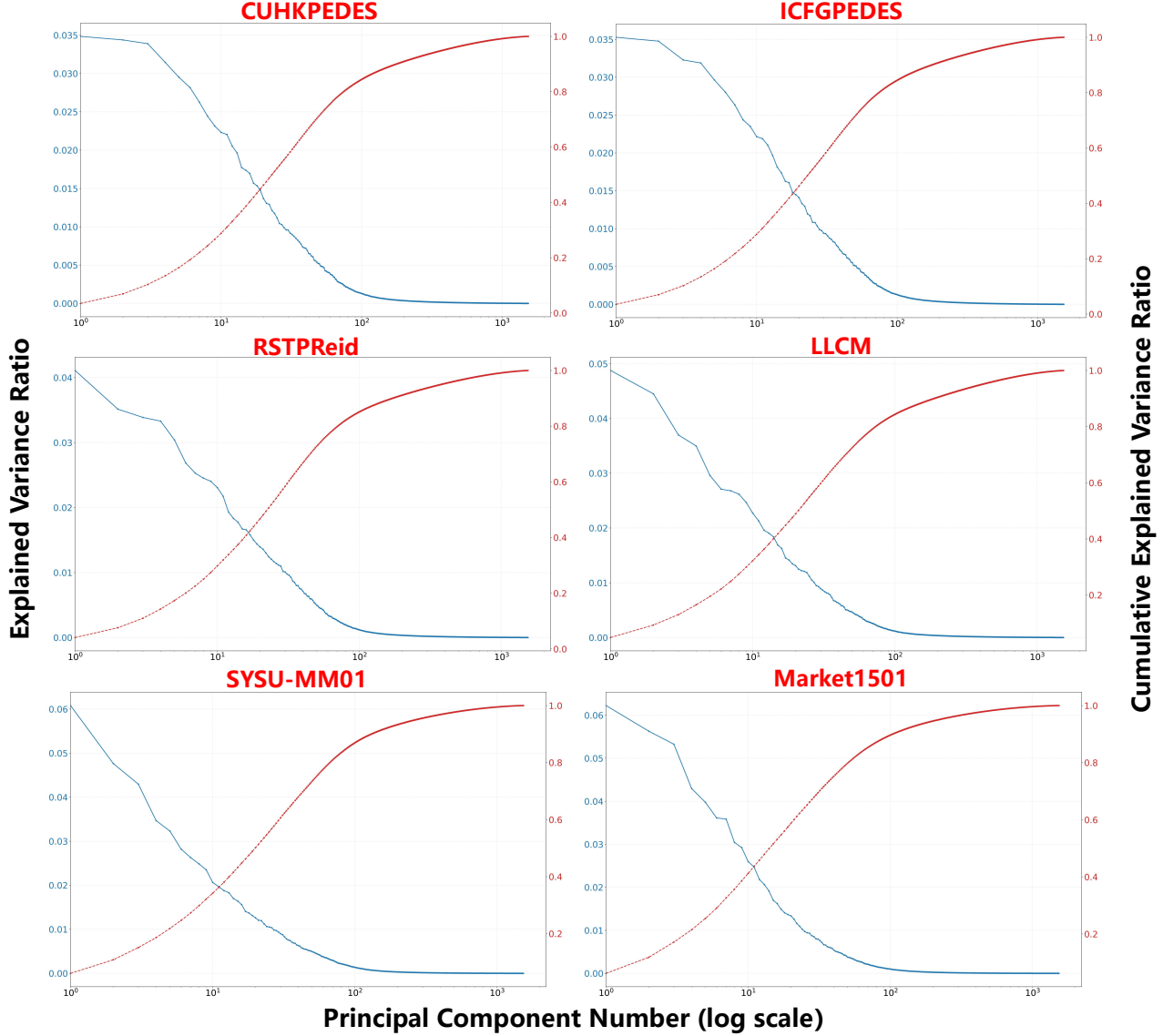


Figure 7. We present the explained variance ratio (blue curves) and cumulative explained variance ratio (red curves) on diverse data distributions. The consistent decay patterns across all trials demonstrate that the observed low-rank structure is a fundamental and dataset-agnostic property of MLLM embeddings.